A TUNABLE EXTENDED DEPTH OF FOCUS MICROSCOPE THROUGH BEAM SHAPE MODULATION INTO AN AXICON LENS

A Thesis

by

FELIPE DE JESUS ZAMBRANO

Submitted to the Office of Graduate and Professional Studies of
Texas A&M University
in partial fulfillment of the requirements for the degree of

MASTER OF SCIENCE

Chair of Committee,	Brian Applegate
Committee Members,	Javier Jo
	Kristen Maitland
	Mark Lenox
Head of Department,	Gerard Coté

August 2015

Major Subject: Biomedical Engineering

ABSTRACT

I propose and demonstrate the groundwork for developing a fluorescence microscopy imaging system by which a Digital Micromirror Device (DMD) and an axicon can be used in combination for remote refocusing of the focal plane while providing high resolution depth profiles, or Axial scans (A-scans), comparable to Optical Coherence Tomography (OCT). Although OCT imaging systems can capture large depth A-scans to buildup high-resolution volumetric images, the information detected by these systems is entirely dependent on the coherent back-scattered light from a sample's structure. Hence, OCT systems are unable to determine a structure's molecular information; however, such information can be acquired from fluorescence systems.

Furthermore, unlike conventional spherical lenses, which have a short depth of focus, the length in which the focal spot begins to diverge to a size greater than $\sqrt{2}$ its spot size, conical lenses like the axicon create a long and narrow depth of focus surrounded by annular rings of lower intensity. Essentially, this focal line, or Extended Depth of Focus (EDF), achieves the same axial resolution as a spherical lens, but has a longer axial length for acquiring A-scans. As a result, a DMD is used to manipulate the size and shape of an illuminated beam pattern, a thin annulus, into the axicon in order to acquire the sample's entire depth profile point-by-point within the EDF. This proposed technique is supported by the point spread function (PSF) measurements from multiple 10 um diameter-sized polystyrene microspheres (fluorescent 540/560 nm), which agree with the mathematical model used in determining the system's axial resolution.

DEDICATION

To my parents, for their everlasting support, and to the lovely “Sue,” whose beauty astounded me at a young age and continues to be a source of inspiration across the world. She’s still looking good despite being about 66 million years old.

ACKNOWLEDGEMENTS

I would like to express gratitude and appreciation to my committee chair, Dr. Applegate, for accepting me into his lab from the very beginning and pushing me to rise to the challenge. His role has been vital in making my graduate school experience a rewarding one. I would also like to thank my committee members, Dr. Jo, Dr. Kristen Maitland, and Dr. Lenox, for their guidance, letting me use their instruments, and supporting me throughout the course of this research.

Thanks also go to my friends, colleagues of the Biomedical Engineering department faculty, and staff for their instruction, everyday help, and making my time at Texas A&M University a great experience.

I am grateful for the student researchers from my lab who supported me in this research, specifically Wihan Kim, Sangmin Kim, Xi Chen, Michael Serafino, and Anna Wisniowiecki. My dearest appreciation goes to Esteban Carbajal, Cory Olsovsky, and Scott P. Mattison for their insightful discussions, helping me out in a moment's notice, and their daily cynical sarcasm.

Finally, I would like to give my greatest thanks to my mother and father (and brothers) for their encouragement and support for the past 2 years in the pursuit of this Master's Degree. Honestly, I could not have accomplished all that I have been able to do without their love and support (and home-cooked meals).

NOMENCLATURE

A-scan	Axial Scan
APD	Avalanche Photodiode
CMOS	Complementary Metal-Oxide Semiconductor
DMD	Digital Micromirror Device
DLP	Digital Light Processing (Software)
EDF	Extended Depth of Focus
FLIM	Fluorescence Lifetime Imaging
FWHM	Full Width at Half Maximum
OCT	Optical Coherence Tomography
PSF	Point Spread Function

TABLE OF CONTENTS

Page

LIST OF FIGURES

Page

LIST OF TABLES

Page

1. INTRODUCTION

The ability to create volumetric images from three dimensional (3D) specimens has relied for a long time on obtaining two dimensional (2D) optical sections through confocal microscopy. In fact, Minsky's invention of the confocal microscope in 1961 is largely responsible for the utilization and advancement of optical sectioning in the microscopy field [1]. Although numerous advances have been made in the last fifty years, the confocal microscope's principle of point-by-point illumination has remained relatively the same. For each focal plane, a point light source is used to illuminate a single point while placing a pinhole aperture in front of the detector in order to physically reject the out-of-focus and pass the in-focus light originating from the object [2]. The optically sectioned image is then built by raster scanning the illumination point across the sample, and the process is repeated for each focal plane within the sample until a volumetric image can be reconstructed from all of the optical sections [3].

Unfortunately, the entire process of sequential scanning on a point-by-point basis for each optical section limits the image acquisition speed [4] thereby limiting the system's temporal resolution and utilization for reliably resolving fast dynamics that occur at the cellular level [5]. To reduce the acquisition time, modifications have been made to the point-by-point illumination process by incorporating high-speed resonant galvonmeters, which barters acquisition speed for image quality [4]. Furthermore, the image quality is dependent on the number and thickness of focal planes within the system's depth of focus. The resolution of the mechanical stage's step increment limits

distance between focal planes, and the mechanical movement of axially moving the sample can cause the appearance of artifacts [6].

An alternative method involves using a combination of cylindrical lenses to expand the laser beam into a line and to pass the illumination and detection light through a slit instead of a pinhole. As a result, multiple image points can be acquired within the specimen by this line-by-line scanning approach as well as increase the acquisition speed. The tradeoff for this method is a decrease in the system's axial resolution because more out-of-focus light passes through the confocal slit [7] .

Likewise, many discrete image points can be simultaneously illuminated by utilizing patterned disks, or scanning disk systems. For example, many pinholes are spread out across the Nipkow disk, and when spun at high speeds, it illuminates many distinct points on the sample while acting as a mask to the emitted light outside of the focal plane [8]. Yet, a drawback to this method is having to physically change out the disks and realign the imaging system when the level of optical sectioning needs to be changed [4].

To remove this common issue of having to physically refocus, several imaging systems have been developed to perform remote refocusing through vari-focus lenses, electrotunable lenses, or accousto-optic modulators. Nonetheless, the image quality in these systems is degraded due to introduced aberrations or suffer from hysteresis [6, 9, 10].

However, an alternative method and modality that can acquire full axial depth scans at a constant resolution and does not have to deal with having to physically change

its focus is Optical Coherence Tomography (OCT). OCT is based on the basic principles of low-coherence interferometry and implements a low-coherence near infrared (NIR) laser as its light source. In Time-Domain OCT (TD-OCT), a beam splitter is used to divide the laser's light into two paths: a reference and a sample arm. The axial scans, or A-scans, that TD-OCT acquires are the interference signals generated by re-combining the reflected light from the sample arm with the reference arm's reflected light. Backscattered light in the sample arm is caused by light reflecting from the microstructures within the sample specimen, whereas the reference arm has light reflecting from a mirror. Since the light in both arms is derived from the same low coherence light source, interference can only occur when both the sample and reference arm have matching path lengths. Thus, making it is possible to determine the depth position from where the sample's backscattered light originated [11]. Although TD-OCT imaging systems can capture large depth A-scans to buildup high-resolution volumetric images, the information detected by these systems is entirely dependent on the coherent backscattered light from the sample's structure and has difficulty in providing molecular information specific to the structure. Fluorescence microscopy is better suited for determining molecular information; however, since fluorescence light is incoherent, it is incompatible to be implemented in OCT systems.

As result, the motivation for this research project has been to develop a fluorescence microscopy imaging system by which a Digital Micromirror Device (DMD) and an axicon can be used in combination for remote refocusing of the focal plane while providing high resolution depth profiles, or A-scans, comparable to OCT.

This research project has explored the effectiveness of using a DMD to manipulate the size and shape of an illuminated beam pattern, a thin annulus, into the axicon in order acquire the sample's entire depth profile point-by-point within an Extended Depth of Focus, or EDF. Ultimately, this research project has demonstrated the groundwork for producing high resolution volumetric images through performing axial sectioning based on the size of the annulus pattern projected from the DMD.

2. THEORY

This section will discuss the functional properties and characterization of the DMD and the axicon due to their integral role in the project's imaging system. In addition, there will be a discussion about the proposed mathematical model for determining the system's axial resolution and the extent of the EDF.

2.1 The Digital Micromirror Device

A promising means for providing flexibility and faster acquisition rates in imaging systems has been to implement Digital Micromirrror Devices (DMDs) as the instrument for creating illumination patterns. A DMD can be described as a Micro-Electro-Mechanical System (MEMS) composed of thousands of switchable micromirrors with two stable states ($\pm 12°$). A +12° pitch signifies that the micromirror is in the "on" state while the opposite is the "off" state [12].

Subsequently, when light is incident to the DMD, light is reflected in these two general directions. Incident light matching the pitch angle of the "on" mirror is reflected at the same angle 12°. All other light is essentially directed away from the +12° by the "off" state mirrors. Yet, the small mirrors arranged in a 2-D array function similar to a diffraction grating, which causes the illumination pattern projected from the DMD to be a diffraction pattern. Light matching the +12° is projected in the diffraction pattern's zeroth order while light not perfectly matching the mirror's angle is directed in the same

general direction as the zeroth order, but with less light intensity. Likewise the same is true with light matching the “off” state angle and its corresponding diffraction orders [13].

By determining which micromirrors turn on and off, it is then possible to create an arbitrary illumination pattern, which can range anywhere from cartoon character shapes to be displayed in projectors or annulus rings as in the scope of this research investigation. Not only are DMDs cost-effective when it comes to optical sectioning, but they also are able to achieve imaging speeds up to 1.6×10^7 pixel/s [14]. Overall, DMDs are an optimal way to create illumination patterns almost instantaneously.

2.2 The Axicon

The first experiments with axicons were performed in 1954 by McLeod, which consisted of characterizing the lens [15]. Since then, a better understanding about the properties of axicons and their applications have been studied, especially with the production of focal lines, or Extended Depth of Focus (EDF). For example, spherical lenses, or “ordinary” lenses, have a short depth of focus, or length in which the beam waist begins to diverge greater than $\sqrt{2}$ of its size at focus. As Figure 1 displays the depth of focus for a spherical lens, it also shows that taking a slice, or cross-section, within the depth of focus, would unsurprisingly reveal a Gaussian beam when illuminated by a Gaussian beam.

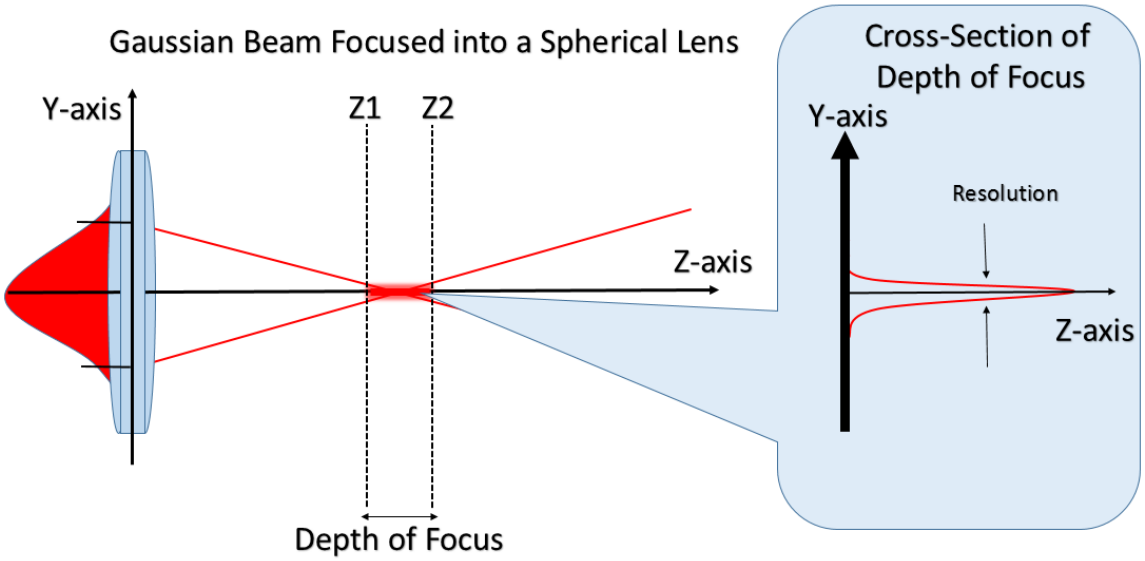

Figure 1: Depth of Focus Characteristics for Spherical Lenses (OBEL 2015)

On the other hand, conical lens such as the axicon, create a long and narrow depth of focus surrounded by annular rings of lower intensity. This is due to all incident rays upon the axicon are deviated towards the optical axis by the same angle, β, and are kept narrow through interference effects [16]. However, if the same Gaussian beam were applied into an axicon, the cross-section would instead show a Bessel beam and with the annular rings surrounding the focal line coinciding with the Bessel beam's side-lobes as illustrated by Figure 2 [17]. This EDF achieves the same axial resolution as a spherical lens, but has a longer axial length, which is desirable when acquiring A-scans.

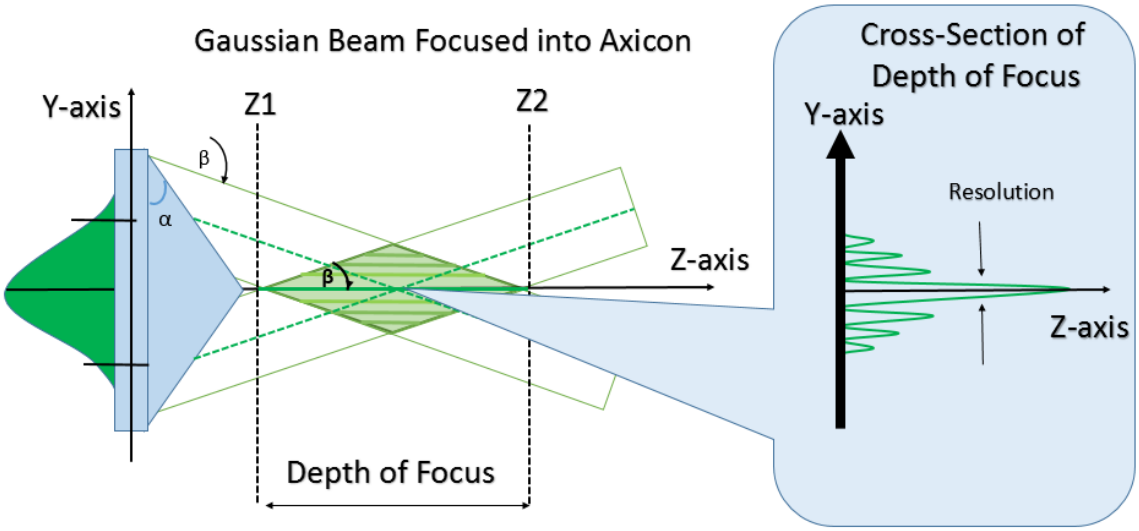

Figure 2: Depth of Focus Characteristics for the Axicon

2.3 Determining the System's Axial Resolution and Depth

Based on the characteristics described for the DMD and the axicon, the plan was to use the DMD to manipulate the size and shape of an illuminated beam pattern, a thin annulus, into the axicon in order to acquire the sample's entire depth profile point-by-point within the EDF. In addition, an annulus of radius, R, passed into the axicon, is focused to Z on the Z-axis based on the following relationship of $Z = \frac{R}{\gamma}$, where γ is a parameter intrinsic to the axicon dependent upon both α and β. The derivation for the focusing relationship and γ are presented in Appendix A. Figure 3 demonstrates how modulating the ring size through the axicon would work. The smallest ring radius possible without warping the beam, Ri, would be passed through the axicon, causing the

beam to be focused by the axicon to position Zi. Zi would mark the starting point of the EDF, and would use the DMD to digitally increase the ring radius in the smallest possible step increments, dR, to the maximum ring radius possible, Ro. ΔR is the difference between Ro and Ri. With the axicon focusing Ro to Zo, the entire focal line will have been imaged point-by-point with a spacing of dZ between points; thereby, having acquired a depth profile without having involved any mechanical stage movement.

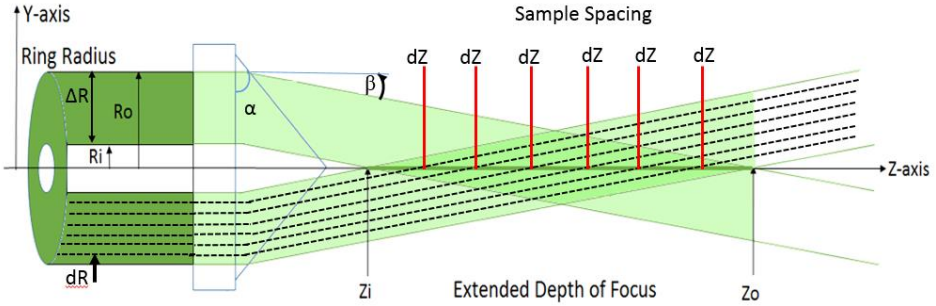

Ri = Smallest Ring Radius Possible
Ro = Largest Ring Radius Possible
ΔR = Ro - Ri

$Z = \frac{R}{\gamma}$

$Zi = \frac{Ri}{\gamma}$, Minimum Point on Focal Line

$Zo = \frac{Ro}{\gamma}$, Maximum Point on Focal Line

ΔZ = Zo – Zi = EDF

dR = Step Increase in Ring Radius

dZ = Spacing of Sample Points within the EDF

Figure 3: Projecting an Annulus Pattern into the Back of the Axicon. The annulus pattern is projected by the light reflected from the DMD. Since all incident light into the axicon is deviated at the same angle, β, the annulus is focused into the focal line. Ri represents the minimum annulus radius that can be focused by the axicon while Ro is the maximum radius. dR is the minimum step increase between the annulus ring radius and ΔR is the difference between Ro and Ri. Zi and Zo respectively represent the beam's position on the Z-axis after having been focused by the axicon and their difference is equal to the focal line's length. dZ represents the sample spacing when measuring point-by-point within the EDF.

Figure 4 is the proposed optical design for implementing the theory presented in Figure 3. The following properties lead to the mathematical model for determining the length of the EDF. With the digital image inputted to the DMD, the pattern goes from a pixel representation to a physical representation with each mirror the size of 12.8 um. Since the length of the EDF is the difference between Zo and Zi, which are refracted from Ro and Ri respectively, ΔR represents this difference in terms of ring radius. When the light source is incident with the DMD, only the light reflected from the "on" state mirrors is projected as a diffraction pattern to L1. The iris following L1 is meant to spatially filter out all diffraction orders other than the zeroth order. Together, L1 and L2, serve to relay the illumination pattern into the axicon and de-magnify the annulus pattern by a ratio of (F2/F1). At the axicon, the annulus is refracted by γ and creates the 1st focal line at (R,Z). Because the axicon is a poor collection optic, the pattern is relayed again by F3 and F4 and de-magnified by a factor of $(F4/F3)^2$ since axially relaying has a square dependence. The resulting focal shift, or length of the EDF can be calculated by using Equation 1, where ΔR = Max Ring Radius – Min Ring Radius

Equation 1

$$\frac{12.8\frac{um}{Pixel} * (\Delta R\ Pixels) * (\frac{F2}{F1})}{\gamma} * \left(\frac{F4}{F3}\right)^2 = EDF\ or\ Focal\ Shift\ (um)$$

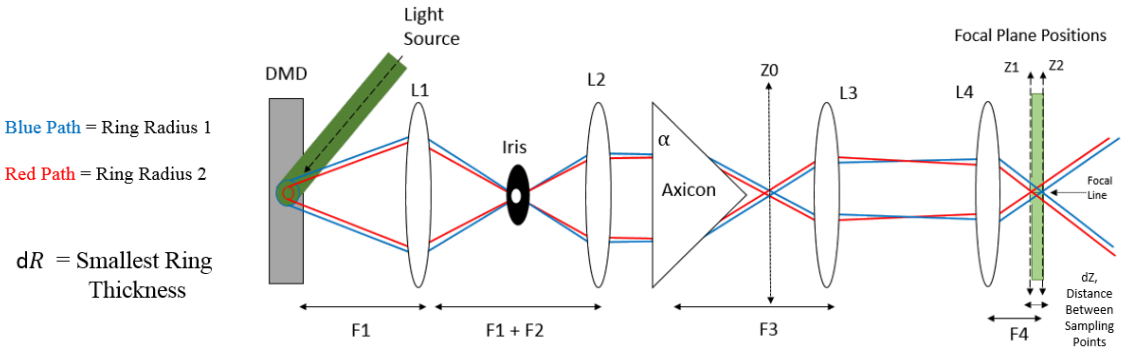

Figure 4: Theoretical Design for Determining the System's Axial Resolution and EDF.

Similar to Equation 1, Equation 2 determines the system's axial resolution by using dR, denoting thickness of the annulus and the smallest change detectable in ring radius length, instead of ΔR. dR is necessary since it will define the distance between sequential points within the EDF, dZ, as well as they system's theoretical ability to resolve between them.

Equation 2

$$\frac{12.8\frac{um}{Pixel} * (\delta R\ Pixels) * (\frac{F2}{F1})}{\gamma} * \left(\frac{F4}{F3}\right)^2 = EDF\ or\ Focal\ Shift\ (um)$$

3. METHODS

The experimental fluorescence microcopy imaging system implemented a DMD (Texas Instruments 0.55 XGA) to generate ring patterns. These patterns were relayed through an axicon (Edmund Optics #83-789) in order to provide axial sectioning. Figure 5 displays the schematic of the optical components used in the completed imaging system.

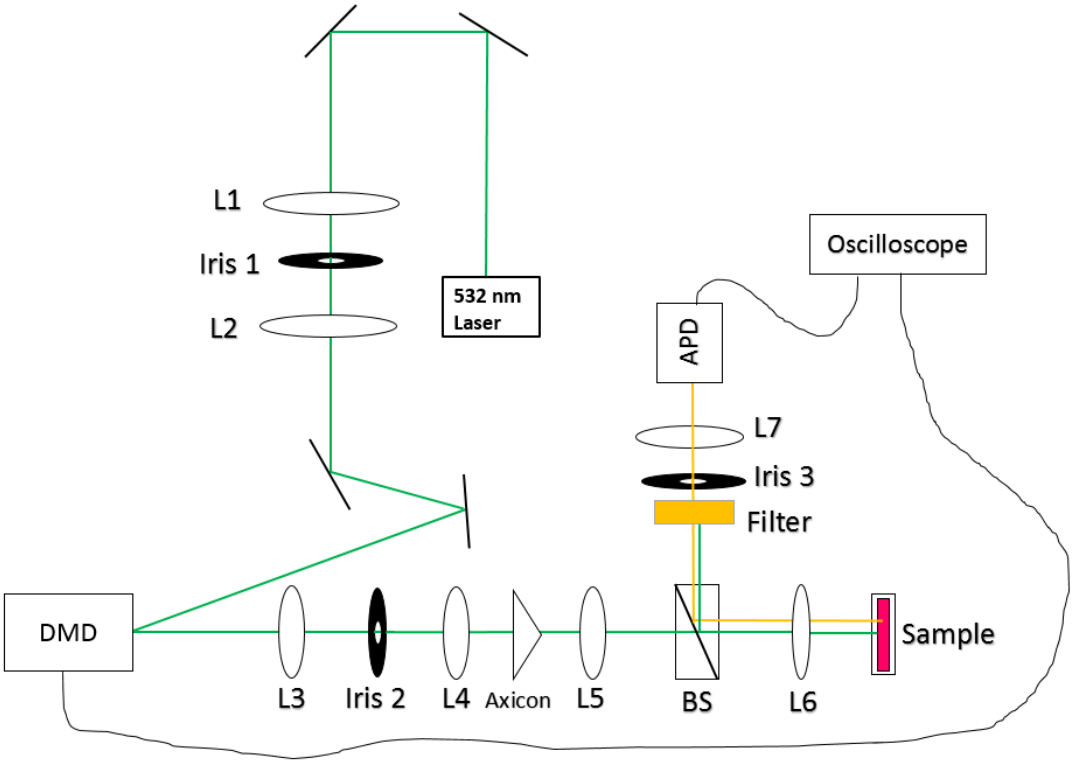

Figure 5: Schematic Diagram of the Proposed Imaging System. The effective focal lengths for the following lenses are as follows: L1=40mm, L2=100mm, L3=75mm, L4=30mm, L5=40mm, L6=20mm, L7=45mm.

3.1 Construction of the Imaging System

The source laser was an Advanced Optical Technology Ltd (AOT) laser with an operating wavelength of 532 nm, a pulse duration of 1 ns, and a pulse rate of 50 kHz. As illustrated in Figure 5, the first set of optical components the beam comes in contact are L1, Iris 1, and L2, which serve to expand the beam's size in order to completely illuminate the DMD. From L2, the beam is passed onto the DMD matrix at a sharp 12° incidence angle in order to match the DMD's large ±12° axis displacement [18]. In having the incident angle equal to the mirror's positive displacement angle, the zeroth order diffraction pattern is reflected along the optical z-axis.

The DLP5500 DMD is part of the 0.55 XGA chipset series from the Texas Instruments (TI) DLP5500 LightCommander development kit [19]. The specifications for this particular DMD are available in Table 1.

Table 1: Specifications for the DLP5500 DMD [19]

DLP5500 DLP® 0.55 XGA Series DMD Specifications	
Illumination size	22.30 mm x 32.20 mm
Array Mirror Size;	1024 x 768 Micrometer sized mirrors
Micromirror Pitch	10.8 um
Material	Aluminum
Wavelength Use	Broadband Visible Light; 420-700 nm
Micromirror Tilt Angle	±12° relative to flat screen
Pattern Frame Rate	Up to 5000 Hz for Binary Pattern (on-off); Used 60 Hz

Table 2 shows the losses in average power changes occurring though the system. The greatest change in average power occurs after the beam is reflected from the DMD to L3 and its diffraction pattern is spatially filtering by Iris 2. This loss of power is due to the small number of the micromirrors being placed in the "on" position to create the annulus pattern while the rest of the light reflected from the "off" position mirrors is lost [20]. Further power is lost due to the multiple diffraction orders created from the micromirrors acting as diffraction gratings as discussed in Section 2.1. Fortunately, the zeroth order of the diffraction pattern carries the highest average power whereas the power exponentially decreases among the higher diffraction orders [13]. Even though the 1st and 2nd diffraction orders carry a lower power compared to the zeroth order, they do interfere with the illumination pattern after being imaged by L4 and cause further

distortion when passed onto the axicon. Therefore, Iris 2 was added to the system to help spatially filter out all of the annulus projections, except for the zeroth order pattern.

Table 2: Specifications of the Optical Components used in the Imaging System

Specifications of Optical Components	
Before L1	38.71 mW
Between L2 & DMD	13.43 mW
Between Iris 2 & L4	180.4 uW
At Sample	7.908 uW

After Iris 2, the zeroth order annulus projection is negatively magnified by L4, and collimated to the axicon whose specifications are available in Table 3. Even though the axicon focuses into a focal line of a 1st-order Bessel-Gauss beam, the working distance from the axicon falls too close the axicon's tip to effectively image a sample. Thus, it is necessary to relay the beam onto L5 so that it can later be focused with a large enough working distance away from L6, which focuses onto the sample.

Table 3: Specifications for the Axicon Lens [21]

25.4 mm Diameter Axicon NT83-789 Specifications	
Apex Angle	130°
Axicon Angle, α	25°
Coating	Visible: 425-675 nm

3.2 Characterization of the Annulus Pattern from the DMD

As it was aforementioned, the DMD is a matrix of micrometer-sized mirrors, which control the illumination pattern based on their on-off state. The DLP LightCommander software designates the on-off state for each mirror according to the binary value for each pixel composing the desired pattern image as in Figure 6. With an image size of 1024 x 768, each pixel has a corresponding mirror; thus, making it possible to arbitrarily select the annulus size and thickness within DMD's operating area.

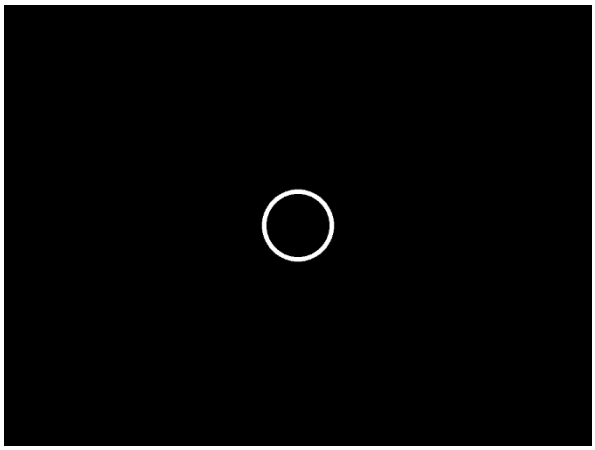

Figure 6: Example of a 1024 x 768 Image Configured into the DMD

A Mightex complementary metal-oxide semiconductor (CMOS) camera was used to image the beam after the axicon to verify the system's alignment. Figure 7 depicts how the inputted pattern would appear if the system were misaligned and subsequently corrected.

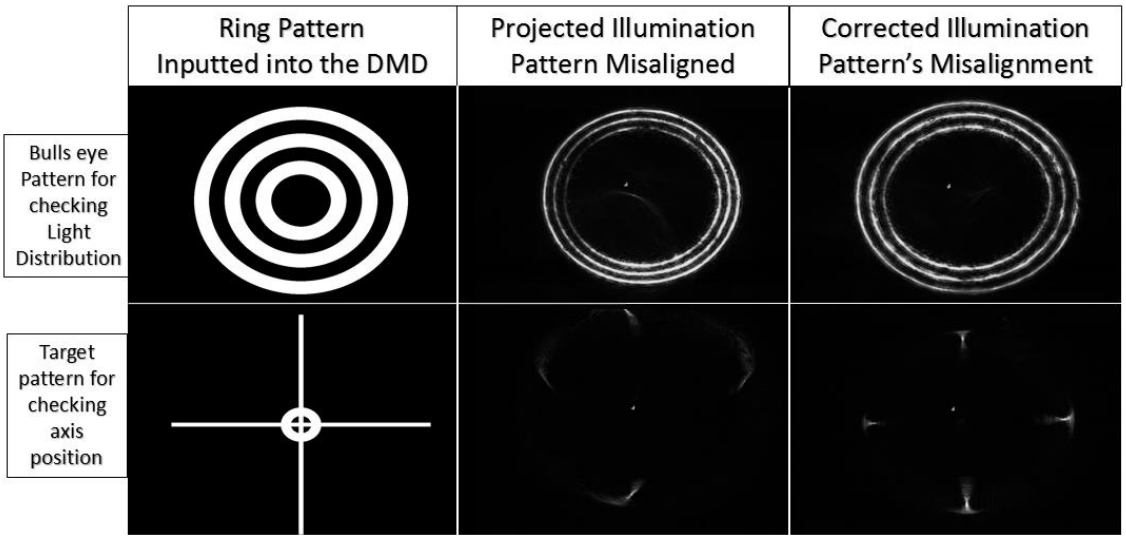

Figure 7: Examples of DMD Patterns Used for Checking System's Alignment

To determine the limits of detection in both size and thickness for the annulus pattern, the CMOS camera was placed at the sample's location as exemplified in Figure 8. The green and red ray tracing represent the optical path for the smallest ring size (red) and the largest (blue) to be detected by the CMOS. Although Figure 8 was similarly used in Section 2.3 for describing the optical path for determining the focal shift, it has been updated with the system's corresponding lenses. Equation 1 will use the difference between the two ring limits to determine the focal shift, or the length of the EDF while Equation 2 will use the ring thickness for establishing the system's axial resolution.

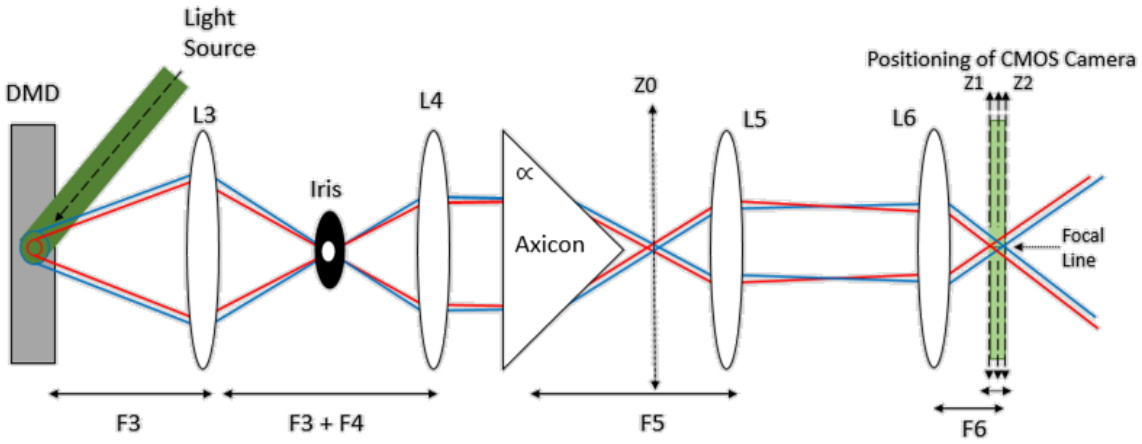

Figure 8: Schematic Diagram for Imaging the Annulus Pattern Limits

3.3 Development of the Collection Arm

Figure 9 remains much the same as in Figure 8, except for the addition of the optical components used for collecting the sample's emitted fluorescence. The collection components are the a 1 inch beam splitter, a 550 long pass emission filter, Iris 3, focusing lens, L7, and the Avalanche Photodiode (APD). The initial sample of choice was a 500 uM solution of Rhodamine 6G encased within a pair of thin coverslips (<150 um). The sample's maximum emission wavelength when excited at 532 nm is 590 nm [22].

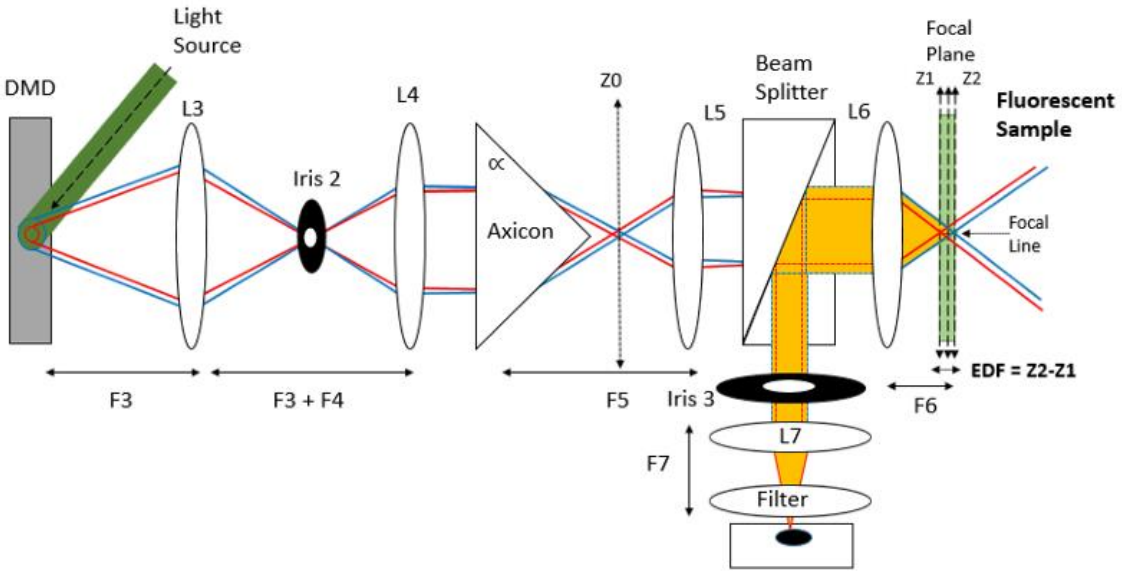

Figure 9: Schematic Diagram of the Collection Arm.

A 550 nm long pass emission filter was selected to prevent the bleed-through of reflected 532 nm light from the sample into the detector. To ensure the least amount of any bleeding from either the 532 nm or other ambient light, the filter was placed as close as possible to the APD. Additionally, the Ocean Optics USB-4000 spectrometer was briefly placed at the APD's location in order to measure the sample's emitted wavelength and determine the filter's effectiveness. Figure 10 displays the spectrometer's results for both Rhodamine 6G and FluoSphere microsphere samples. Clearly, the filter was working properly since there was a negligible presence of 532 nm light within the spectrum. Moreover, there was not a significant difference in the fluorescence emission wavelengths between the microspheres and the Rhodamine 6G sample.

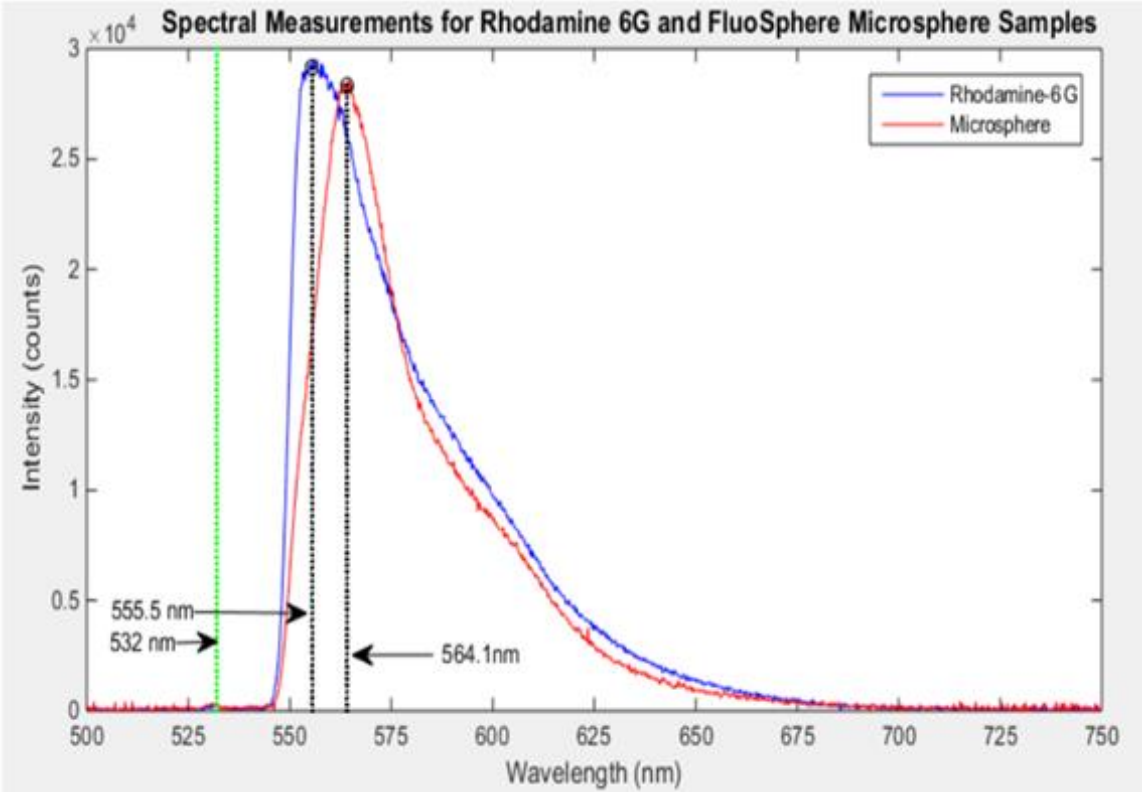

Figure 10: Spectral Measurements for Rhodamine 6G and FluoSphere Microsphere Samples

3.4 Rhodamine 6G and FluoSphere Microsphere Sample Preparation

Figure 11 illustrates the preparation and imaging for the Rhodamine 6G sample. Part A of the figure is a visual representation of how the sample was prepared by encasing a droplet of the solution within a 1.5 cm diameter ring of Vaseline onto the base coverslip. To the left and right of the ring (about a 1/3 of the base coverslip's length), a coverslip piece was attached to the coverslip using Vaseline. Finally, the top coverslip was placed on top of the two center two coverslip pieces and the Vaseline ring.

Pressing down on the coverslips caused the Rhodamine droplet to spread out and conform to the Vaseline ring without any bleeding. In this configuration the Rhodamine sample has a thickness matching the coverslip, ~ 150 um, which is also the sample's expected EDF length. Part B depicts a generalized ray tracing of the expected focal positions from L6 depending on the annulus's radius length.

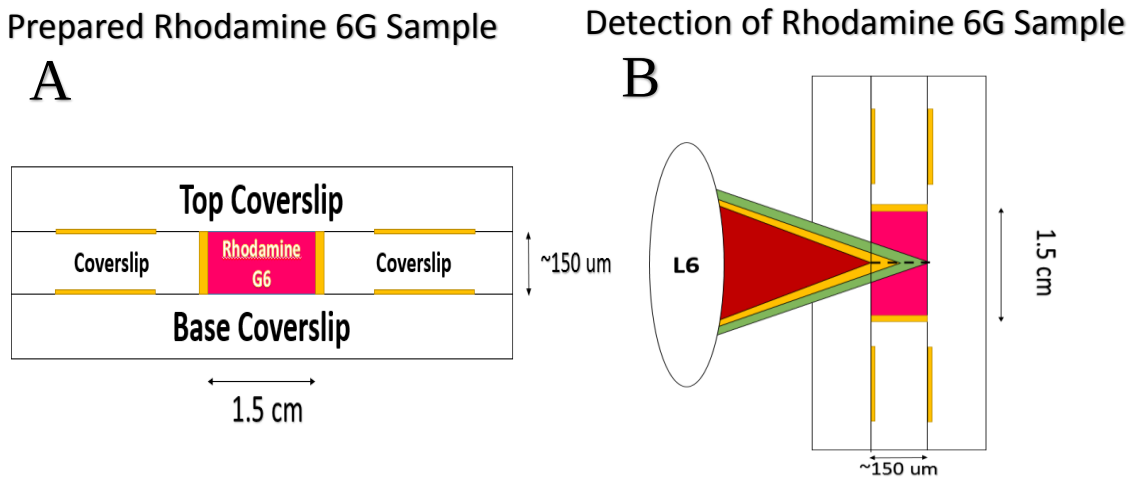

Figure 11: Preparation and Detection of Rhodamine 6G Sample

The Rhodamine 6G samples serves to explore the effects when imaging a sample containing a homogenous distribution of fluorophores. On the other hand, the FluoSphere microsphere samples were prepared in a manner to test a sparse distribution of fluorophores with the goal of determining the system's axial resolution. Preparation for the microspheres initially involved sonicating them in a 100 MHz ultrasonic bath for five minutes in order to suspend them in solution and avoid aggregation. Once dissolved in solution, the concentration of microspheres in solution was 3.6 x 10^6 beads/mL, C0.

After adjusting the protocol from Bangs Laboratories, the following procedure was performed to dry microspheres onto a microscope slide. First, 0.5 mL of the solution, V0 was drawn and added to a test tube. The tube was centrifuged at 2,500 rpm for 5 minutes in order to concentrate the beads to the tube's tip. The supernatant was drawn out and disposed of followed by a re-suspension of the microspheres in a solution of 25% ethanol and 75% water. The tube was again centrifuged at the same speed and length of time followed by removing the supernatant as before. This entire process of centrifugation and removal of supernatant was repeated for 50%, 75%, and 100% ethanol:water solutions [23].

Once the microspheres were suspended in the 100% ethanol solution, the volume was increased to 7 mL, C1, and were exposed to another ultrasound bath for 5 minutes. Upon the microspheres being completely dissolved in solution, 1 uL of the aqueous solution was drawn and placed onto a microscope slide to roughly cover a 1.5 cm spot diameter. Roughly 5-6 of these spots were spread across the microscope slide's surface. To let the ethanol evaporate and leave behind only the microspheres, the microscope slide was placed in a vacuum hood and prevent photobleaching. For the remaining microspheres in solution, half of its volume (3.5 mL) was placed into another tube and had 3.5 mL of ethanol added to it for a new microsphere concentration, C2, and volume of 7 mL. C2 underwent the same procedure that C1 undertook for sonication and being placed on a microscope slide. Figure 12 offers a visualization of the described dilution process taken from C0 to C2.

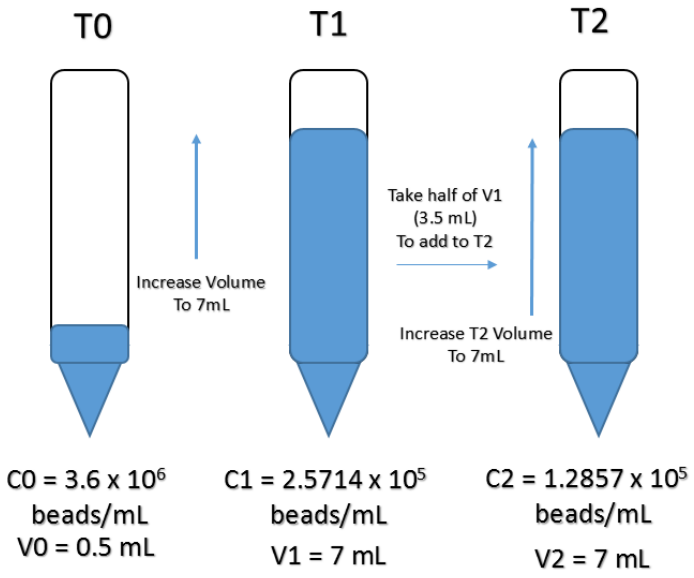

Figure 12: Visualization of Dilution of Microspheres

The distribution of microspheres for each spot concentration can be calculated using Equation 3 for dilution:

Equation 3

$$C_1V_1 = C_2V_2$$

Table 4 lists the number of beads per concentration's spot on the microscope slide, and Figure 13 is an image of the microsphere's distribution from a T2 spot using a light microscope. The image confirms that the microspheres have spread out on the microscope slide as a monolayer (no aggregated beads/clumps) and have a rough 50 – 80 um separation from one another. Hence, the sample has a sparse distribution of fluorophores that will undergo emission when light is focused on or within a single microsphere.

Table 4 : Number of Beads per Spot on Microscope slide and Distribution

Concentration of Microspheres per Spot on Microscope Slide	
T1	2571.4 Beads; 14.56 Beads/mm^2
T2	1285.7 Beads; 7.28 Beads/mm^2

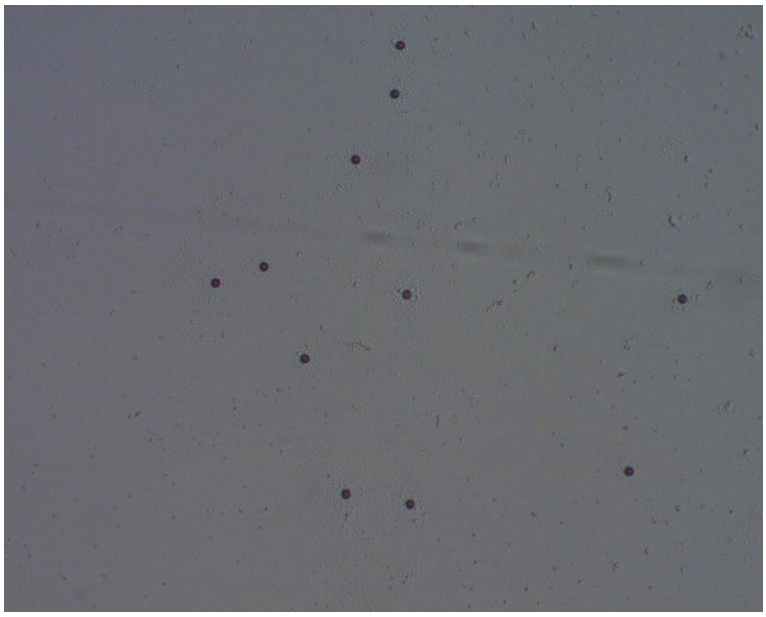

Figure 13: Distribution of Microspheres in Sample T2

3.5 Acquiring and Measuring Sample PSF

The APD used for detecting emitted light was a MenloSystems APD210, and its specifications are listed in Table 5. The APD was connected to an oscilloscope from

which the voltage readings were saved into an excel sheets that could later be processed in Matlab.

Table 5: Specifications for the APD [24]

MenloSystems APD210 Specifications	
Detector Type	Silicon APD
Wavelength Range	400 – 1000 nm
Detector Diameter	0.5 mm
Max Conversion Gain	2.5×10^5 V/W at 1 GHz, 800 nm
Frequency Range (Max)	1 MHz – 1600 MHz
Max Pulse Length	Less than 30 ns

Signal acquisition from either the Rhodamine 6G or microsphere samples relatively followed the same procedure. For instance, determining the sample's focal line length, or distance from which signal was being detected, involved using a single annulus frame pattern for the DMD to project. By having this stationary pattern, which is later referred to as the "focal ring," Newport stages could be manually controlled in searching for the pattern's focal spot position. The stage of primary stage of interest was the axial z-axis stage since it would allow the sample to be moved to the pattern's focal spot position. Once signal appeared on the oscilloscope, the axial position was recorded, Z2, and the stage continued to slowly progress in the direction providing a steady rise in voltage being displayed on the oscilloscope. When it appeared that the climbing voltage

waveform had reached its peak and began to drop-off, the position was recorded as the annulus's focal spot position, or Z1. Afterwards, the stage continued to move until the oscilloscope stopped showing any voltage signal, at which the position was recorded, Z0. Figure 3.10 illustrates this described process, and the difference between the Z2 and Z0 is the length of the EDF, or focal line.

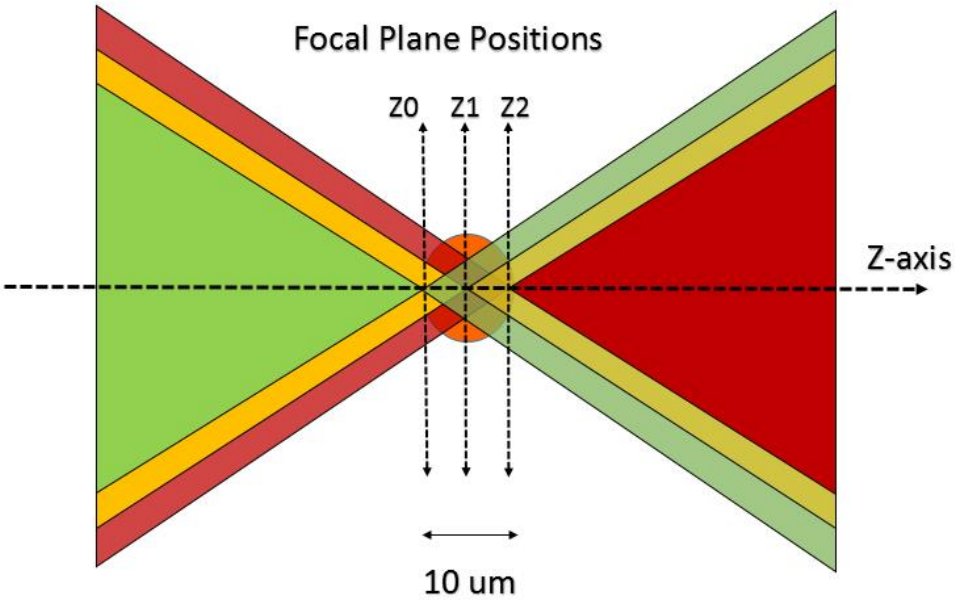

Figure 14: Focal Plane Positions Based on a Single Annulus Ring Pattern.

The z-axis stage was then moved to the recorded Z1 position since this was the location of the pattern's focal spot. To determine the sample's PSF, a sequential series of annulus patterns were outputted from the DMD at a rate of 60 Hz. The number of ring patterns for the DMD to display was selected by adding a pair of rings (2 pixel radius

length difference; one smaller and one larger than the “focal ring”) before and after the “focal ring.” Pairs were added to the focal ring until it was observable on the oscilloscope that these additional rings were not contributing any signal; therefore, being focused beyond the extent of the EDF. During these ring-by-ring sequence measurements, the sample was not moved since moving it would shift the sequence and cause a new central “focal ring” to take place and require to restart the ring sequence. Figure 15 illustrates how each sequential ring pattern is passed through the sample’s EDF and the effect of moving the sample during the ring-by-ring imaging sequence. The ring occurring at the focal plane in part B is the dubbed “focal ring.”

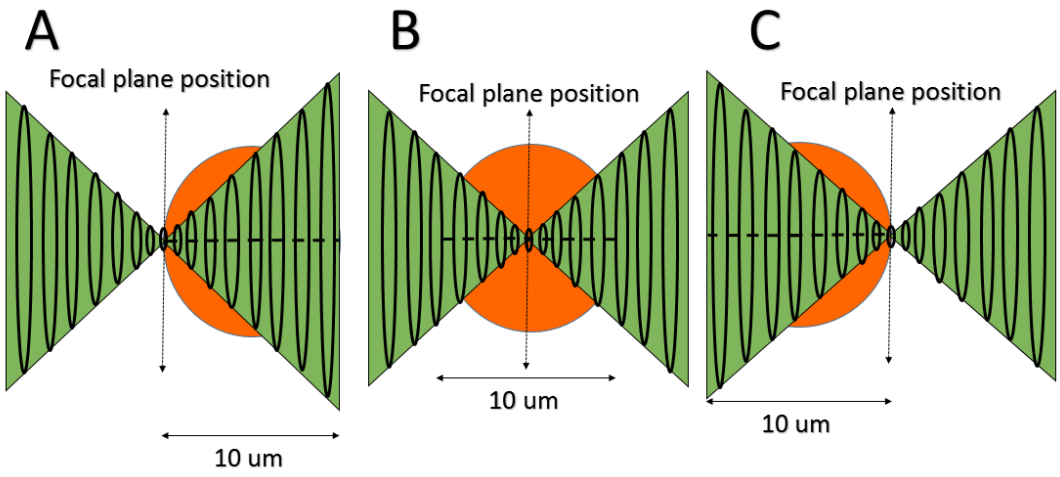

Figure 15: Passing Sequential Ring Sizes through the Sample

4. RESULTS AND DISCUSSION

4.1 Determining Theoretical Limits

In testing the imaging system's limits based on the size and thickness of the rings inputted into the DMD, the following information was determined. The thinnest ring thickness that did not experience any changes to the ring shape was a 1 pixel thickness. However, as Figure 16 demonstrates, the CMOS had difficulty in detecting the ring pattern when positioned 700 um from the pattern's focal spot, and the ring was hardly seen when the CMOS was position 100 um from the pattern's focal spot. Images of the ring shape would have been taken at the pattern's focal spot for additional comparison, but the CMOS was unable to provide resolved images of any of the rings at that specific position (a blurry spot was seen by all patterns). Since the 1 pixel thickness was difficult to detect, the 2 pixel thickness was selected as the ring thickness for all ring patterns to follow. By applying the 2 pixel thickness to Equation 2, the system's theoretical axial resolution for the system is 9.86 um.

Equation 2

$$\frac{12.8*(Ring\ Thickness)}{\gamma} * \left(\frac{F4}{F3}\right)\left(\frac{F6}{F5}\right)^2 = \frac{12.8\ (\frac{um}{Pixel})*(2\ Pixel)}{0.26} * \left(\frac{30}{75}\right)\left(\frac{20}{40}\right)^2 = 9.86\ um$$

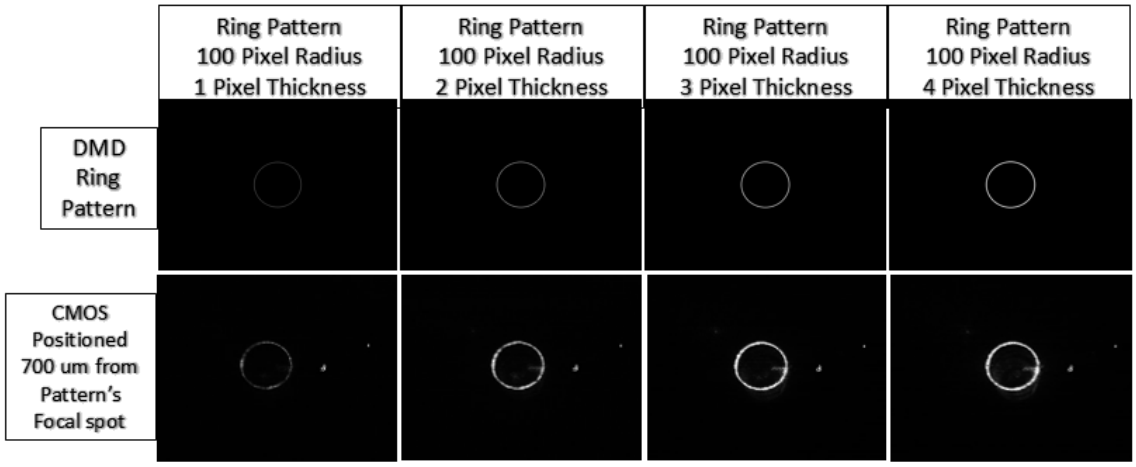

Figure 16: Ring Thickness of 1 to 4 Pixels

In addition, the largest ring size with a 2 pixel thickness that the DMD could display without disrupting the ring's shape was a pixel radius of 355. As shown by Figure 17, rings with a radius longer than 379 pixels resulted in their shape being clipped since the ring's diameter was larger than the DMD's area (768 pixels). Even though rings with a radius between 379 and 356 could be displayed by the DMD, they unfortunately experienced a similar clipped effect towards top and bottom edges due to the incident beam not being large enough to fully illuminate the pattern. At a pixel radius of 355, the clipped effect became non-existent and featured a better distribution of light throughout its pattern.

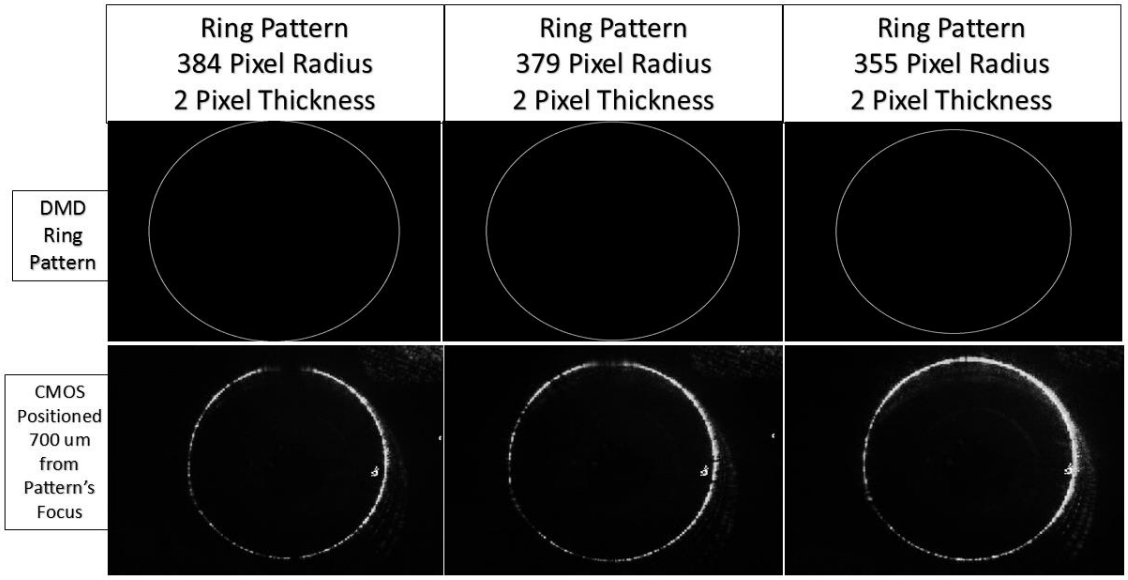

Figure 17: Ring's with a Radius Larger than 355 Pixels

Conversely, the smallest ring size with a 2 pixel thickness that the DMD could completely display was a pixel radius of 95. Figure 18 depicts the surprising effect of having a radius less than 95 pixels. At 94 pixels, the ring is almost complete, but is missing two small parts towards its top. As the radius diminishes in size, the ring begins to devolve around its lower right quadrant and work its way around until it is completely unrecognizable at a radius of 30 pixels. However, this devolution in shape is due to the projected ring being physically blocked by the axicon's tip. For example, at the 50 pixel radius, approximately the top half of the ring is displayed, whereas the bottom half is filled in by 95 pixels radius. Thus, making the 95 pixel radius not only the minimum length for displaying a complete illuminated ring pattern, but also length needed to bypass the axicon's tip.

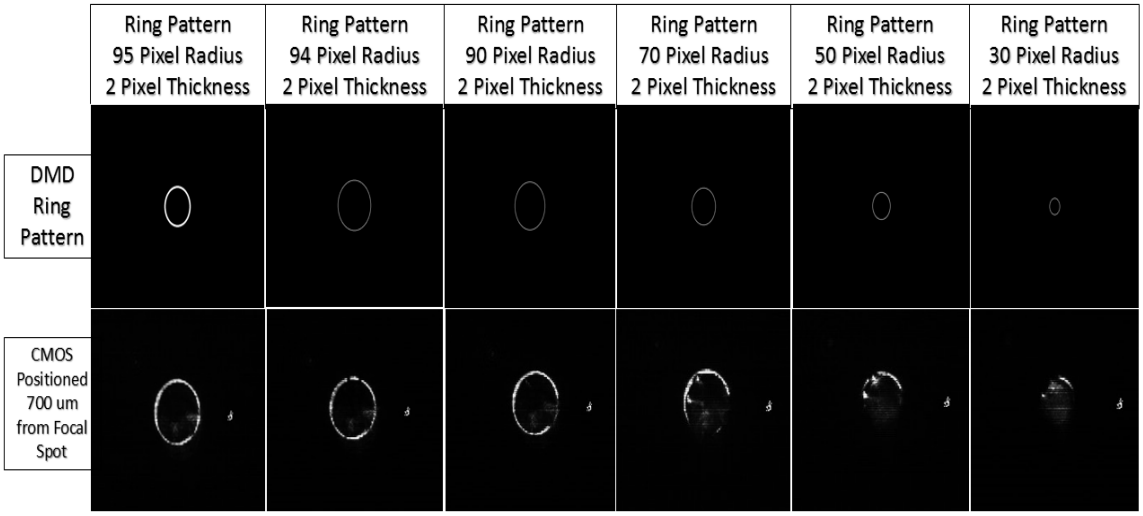

Figure 18: Effects of Rings with a Radius Less than 70 Pixels

With the minimum and maximum ring sizes determined, the theoretical maximum length for the focal line, or EDF, can be determined using equation 1 again.

Equation 1

$$\frac{12.8*(Max-Min\ Pixel\ Radius)}{\gamma} * \left(\frac{F4}{F3}\right)\left(\frac{F6}{F5}\right)^2 = \frac{12.8\left(\frac{um}{Pixel}\right)*((355-95)Pixels)}{0.26} * \left(\frac{30}{75}\right)\left(\frac{20}{40}\right)^2 =$$

$$= 1281.97\ um$$

As a result, the theoretical maximum length possible for the EDF is 1281.97 um.

4.2 PSF Measurements for Rhodamine 6G Sample

Figure 19 is the PSF of the Rhodamine 6G sample based on the sequence of ring patterns with a radius length of 122 to 179 pixels and a "ring focus" radius 153 pixels. As mentioned in section 3.5, the "focal ring" radius of 153 pixels means that it was the

only inputted ring pattern into the DMD while the Rhodamine sample was moved using the Newport stages to record the sample's EDF. After having determined the length of the focal line, the stage was positioned to where the maximum voltage had been recorded. It was at this position that the entire ring sequence from 122 to 179 was placed in sequence and each ring's corresponding voltage was recorded to construct Figure 19. This plot describes relationship between the ring radius length and the amount of fluorophores emitted by the sample, which are transduced into voltage by the APD.

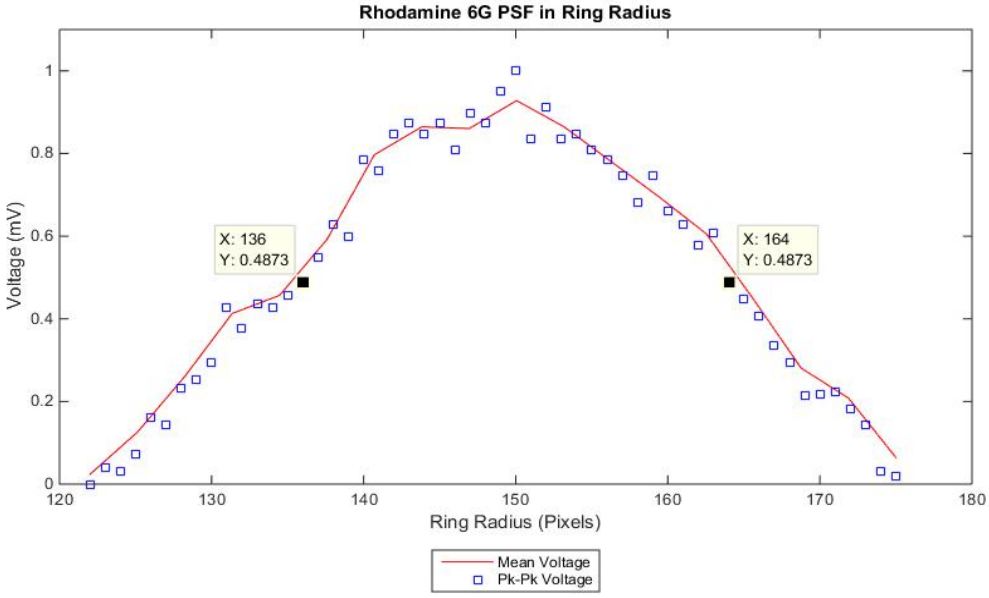

Figure 19: PSF of Rhodamine 6G Sample in Ring Radius Length

Figure 20 depicts the same voltage relationship from Figure 19, but it has been plotted in terms of the focal line's length. By measuring the Full-Width of the plot at Half the Maximum voltage (FWHM), which is meant to describe the sample's PSF.

Consequently, the sample's FWHM is 359.4 um, which is much greater than the expected value of 150 um, the coverslip's width. The reason behind the large PSF is due to the sample's composition of being a homogenous distribution of fluorophores. The collection optics are operating under the assumption that it is collecting only the light that is in focus within the sample. However, since the sample has the fluorophores equally distributed in all directions within the sample's length (150 um), the out-of-focus light is interacting with the fluorophores and contributing to the collected signal. This additional gain in signal is inherent to the sample and cannot be removed from a sample with this homogenous distribution. Nonetheless, by having a sample with a sparse distribution of the fluorophores, as in the case with the microsphere sample, the out-of-focus light should be mitigated.

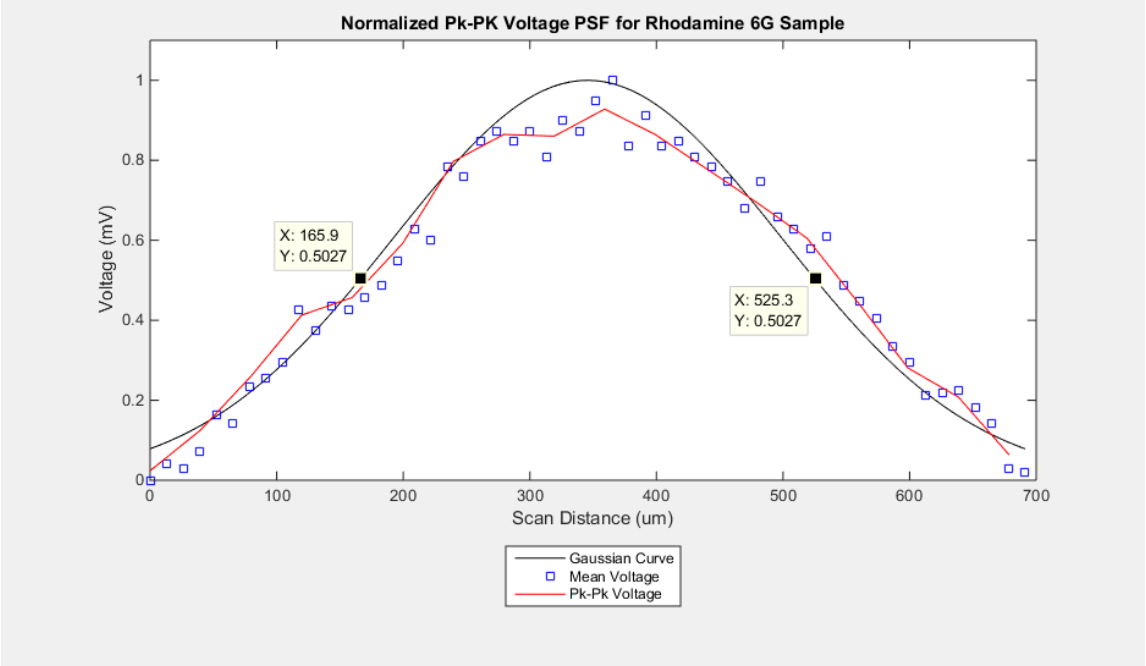

Figure 20: PSF of Rhodamine 6G Sample Plotted Over EDF Distance

4.3 PSF Measurements for Microsphere Samples

Figure 21 is the PSF of the T2 concentration microsphere sample based on the sequence of ring patterns with a radius length of 160 to 183 pixels. The method for acquiring this plot was the same as described for the Rhodamine sample in the previous, but with the "ring focus" pattern being set to a radius of 172 pixels. Unfortunately, the sample did suffer from having some of out-of-focus light being added to the signal. But it was possible to reduce its effect by adding in an iris, Iris3, between the beam splitter and L3 in the system. By reducing the diameter of the iris, the numerical aperture (NA) of the collection optics is decreased, and in turn increasing the depth of focus. Multiple iris diameters where tested, but it was finally the Iris diameter of 1.3 cm, which created an NA of 0.3, that provided the necessary plot for Figure 21.

The microsphere sample was found to have a FWHM of 12 um. However, since the sample size was roughly equal to the theoretical PSF of the system, it is not accurate to simply compare this result to the expected axial resolution of 9.86 um. Instead, an accurate comparison is the resulting FWHM from the convolution of the theoretical PSF and the sample, assuming a rectangular shape, which results with a 12.40 um FWHM as shown in Figure 22. As a result, this illustrates that the acquired measurements for the microsphere is approximate to its theoretical expectations. Since this sample is the smallest object available that the system can test and has a size approximate to the theoretical axial resolution, this serves as a good approximation of the system's axial resolution. Furthermore, this image demonstrates how the annulus pattern from the

DMD can be used to produce a strong, localized signal without having the need to move the sample via stage control and can be performed remotely.

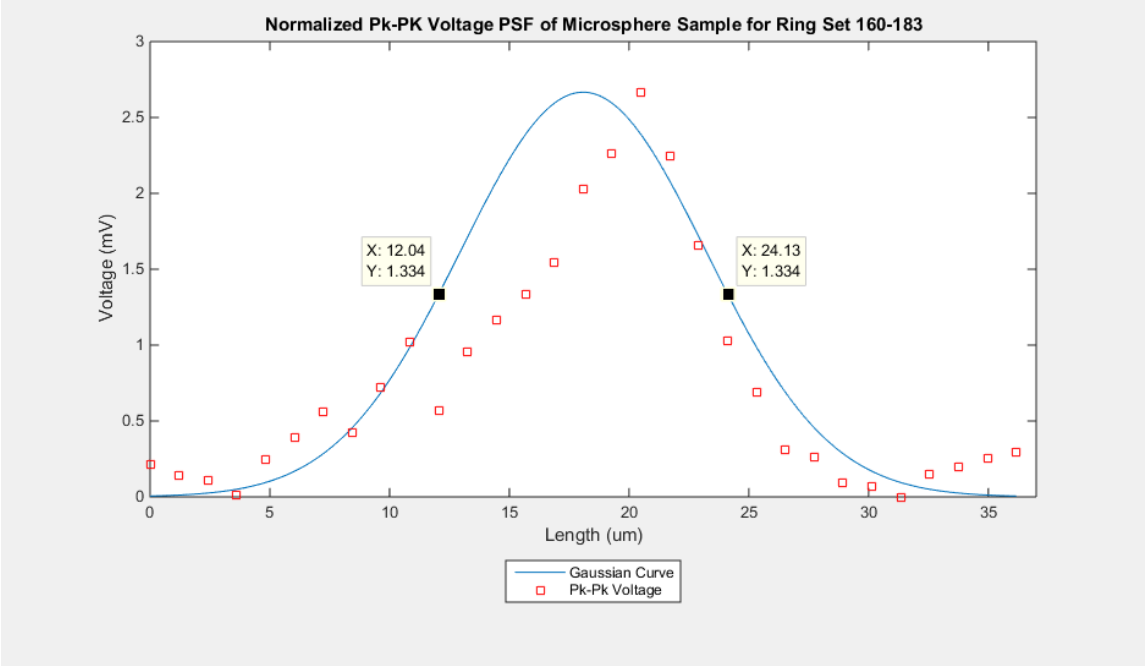

Figure 21: PSF of Microsphere Sample Plotted Over EDF Distance. This image is the forerunner for demonstrating the system's capability in acquiring unique voltages at each position within the focal line.

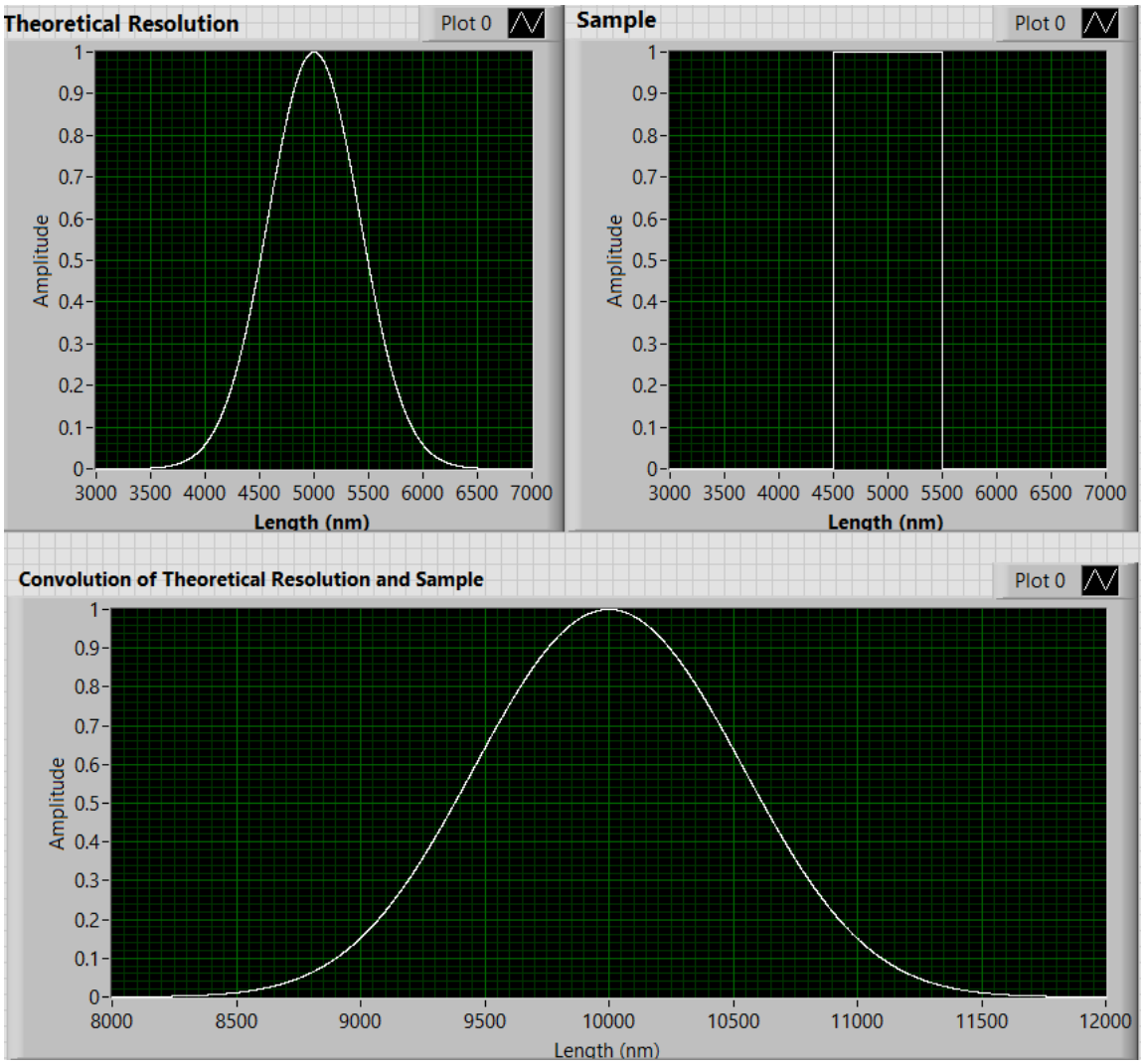

Figure 22: Convolution of the Theoretical Axial Resolution and Sample for a FWHM of 12.4 um.

5. CONCLUSION

The experimental results demonstrate that the imaging system was able to acquire an excellent PSF for the microsphere sample. As a result, the system has been able to not only demonstrate axial sectioning within the sample's EDF but also an innovative new method for the remote refocusing of the focal plane. A functional extension of the system would be to introduce a pair of galvonmeters to produce a raster scan at each position of the sample; thus, enabling a volumetric image to be produced This method could be incredibly helpful among the fluorescent modalities such as Fluorescence Lifetime Imaging (FLIM) since they very little, if any, axial sectioning in their systems due to their long depth of focus. By allowing these systems to operate within the EDF, they would be able to provide higher resolution and greater detail to their volumetric images.

Overall, this project has completed its first goal in its pursuit of producing high resolution volumetric images by providing supported evidence that the system is capable of performing axial sectioning based on the size of the annulus pattern projected from the DMD.

REFERENCES

1. Minsky, M., *Microscopy apparatus*. 1961, Google Patents.
2. Pawley, J.B. and R.B.R. Masters, *Handbook of Biological Confocal Microscopy, Second Edition.* Optical Engineering, 1996. **35**(9): p. 2765-2766.
3. Poher, V., et al., *Optical sectioning microscopes with no moving parts using a micro-stripe array light emitting diode.* Optics Express, 2007. **15**(18): p. 11196-11206.
4. Martial, F.P. and N.A. Hartell, *Programmable illumination and high-speed, multi-wavelength, confocal microscopy using a digital micromirror.* PLoS One, 2012. **7**(8): p. e43942.
5. Oron, D., E. Tal, and Y. Silberberg, *Scanningless depth-resolved microscopy.* Optics Express, 2005. **13**(5): p. 1468-1476.
6. Smith, C., et al. *Extended depth-of-field microscopy*. in *BiOS*. 2010. International Society for Optics and Photonics.
7. Callamaras, N. and I. Parker, *[10] Construction of line-scan confocal microscope for physiological recording*, in *Methods in Enzymology*, P.M. Conn, Editor. 1999, Academic Press. p. 152-169.
8. Nakano, A., *Spinning-disk Confocal Microscopy — A Cutting-Edge Tool for Imaging of Membrane Traffic.* Cell Structure and Function, 2002. **27**(5): p. 349-355.

9. Botcherby, E.J., et al., *Real-time extended depth of field microscopy.* Optics Express, 2008. **16**(26): p. 21843-21848.

10. Jabbour, J.M., et al., *Optical axial scanning in confocal microscopy using an electrically tunable lens.* Biomed Opt Express, 2014. **5**(2): p. 645-52.

11. Fujimoto, J.G., et al., *Optical Coherence Tomography: An Emerging Technology for Biomedical Imaging and Optical Biopsy.* Neoplasia (New York, N.Y.), 2000. **2**(1-2): p. 9-25.

12. Xu, D., et al., *Fast optical sectioning obtained by structured illumination microscopy using a digital mirror device.* Journal of Biomedical Optics, 2013. **18**(6): p. 060503-060503.

13. Richardson Gratings (Richardson Grating Laboratory), *Diffraction Grating Handbook.* New York. 1999.

14. Dan, D., et al., *DMD-based LED-illumination Super-resolution and optical sectioning microscopy.* Sci. Rep., 2013. **3**.

15. McLeod, J.H., *The Axicon: A New Type of Optical Element.* Journal of the Optical Society of America, 1954. **44**(8): p. 592-592.

16. Burvall, A., *Axicon imaging by scalar diffraction theory.* 2004.

17. Lei, M. and B. Yao, *Characteristics of beam profile of Gaussian beam passing through an axicon.* Optics communications, 2004. **239**(4): p. 367-372.

18. Texas Instruments Staff, *Using Lasers with DLP® DMD technology.* April 2011.Revised May 2015.

19. Staff, T.I.T., *DLP5500 DLP® 0.55 XGA Series 450 DMD*. 2015: Texas Instruments.

20. Hanley, et al., *An optical sectioning programmable array microscope implemented with a digital micromirror device.* Journal of Microscopy, 1999. **196**(3): p. 317-331.

21. Staff, *130° Apex Angle, 25.4mm Dia, VIS 0° Coated Axicon.* 2014 Edmund Optics Inc.

22. Zehentbauer, F.M., et al., *Fluorescence spectroscopy of Rhodamine 6G: Concentration and solvent effects.* Spectrochimica Acta Part A: Molecular and Biomolecular Spectroscopy, 2014. **121**(0): p. 147-151.

23. Bang Laboratories, I., *Drying & Re-Suspending Microspheres*. TechNote 203A. 2013.

24. Staff, *APD 210/310 High Sensitivity Detector Unit.* 2015: MenloSystems.

APPENDIX A: DERIVATION OF γ Value

With Figure 23 as a reference, Light incident upon the axicon is deviated towards the optical axis by an angle, β:

Equation 4

$$\beta = sin^{-1}\ (nsin(\propto)) - \propto$$

Where α is the axicon's cone angle and *n* is the axicon's refractive index

From α and β, γ is determined by applying Snell's law:

Equation 5

$$\boldsymbol{nsin}(\propto) = \ \boldsymbol{sin}(\propto + \beta)$$

Which is simplified to:

Equation 6

$$\gamma = \frac{tan(\beta)}{1 - \tan(\propto)\tan(\beta)}$$

Thus, making γ a parameter intrinsic to the axicon dependent upon both α and *n*. Since the axicon used had α = 25° and *n* = 1.458, γ was determined to be 0.26.

In addition, the following relationship of an annulus of radius, R, passed into the axicon, is focused to Z on the Z-axis by:

Equation 7

$$Z = \frac{R}{\gamma} = \frac{R}{0.26}$$

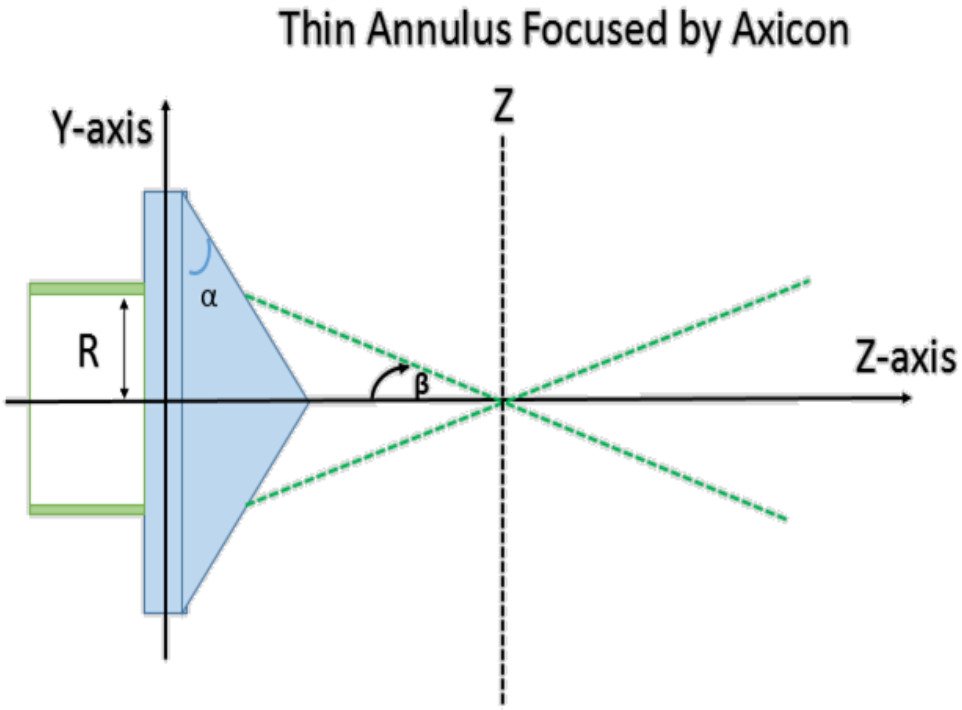

Figure 23: Focusing of an Annulus with a Radius, R, onto the Z-axis at Position Z